

Article

Estimating Daily Global Evapotranspiration Using Penman–Monteith Equation and Remotely Sensed Land Surface Temperature

Roozbeh Raoufi *  and Edward Beighley

Civil and Environmental Engineering, Northeastern University, 360 Huntington Ave., Boston, MA 02115, USA; r.beighley@northeastern.edu

* Correspondence: raoufi.r@husky.neu.edu; Tel.: +1-505-615-5862

Received: 24 August 2017; Accepted: 2 November 2017; Published: 7 November 2017

Abstract: Daily evapotranspiration (*ET*) is modeled globally for the period 2000–2013 based on the Penman–Monteith equation with radiation and vapor pressures derived using remotely sensed Land Surface Temperature (*LST*) from the MODerate resolution Imaging Spectroradiometer (MODIS) on the Aqua and Terra satellites. The *ET* for a given land area is based on four surface conditions: wet/dry and vegetated/non-vegetated. For each, the *ET* resistance terms are based on land cover, leaf area index (*LAI*) and literature values. The vegetated/non-vegetated fractions of the land surface are estimated using land cover, *LAI*, a simplified version of the Beer–Lambert law for describing light transition through vegetation and newly derived light extension coefficients for each MODIS land cover type. The wet/dry fractions of the land surface are nonlinear functions of *LST* derived humidity calibrated using in-situ *ET* measurements. Results are compared to in-situ measurements (average of the root mean squared errors and mean absolute errors for 39 sites are 0.81 mm day^{-1} and 0.59 mm day^{-1} , respectively) and the MODIS *ET* product, MOD16, (mean bias during 2001–2013 is -0.2 mm day^{-1}). Although the mean global difference between MOD16 and *ET* estimates is only 0.2 mm day^{-1} , local temperature derived vapor pressures are the likely contributor to differences, especially in energy and water limited regions. The intended application for the presented model is simulating *ET* based on long-term climate forecasts (e.g., using only minimum, maximum and mean daily or monthly temperatures).

Keywords: evapotranspiration; remote sensing; MODIS; canopy evaporation; soil surface evaporation; transpiration; vegetation cover fraction; wet fraction; AmeriFlux

1. Introduction

Evapotranspiration represents the summation of coupled processes controlling evaporation from impervious, soil, vegetation and open-water surfaces and transpiration from plants. Although it is a major component of the hydrologic cycle, with roughly 60–65% of all precipitation over land being removed from the terrestrial water cycle through *ET* [1–4], it is hard to quantify because of the many different factors influencing the many *ET* processes [5]. To further our understanding of *ET* and support the development and application of process models, in-situ measurement networks encompassing varied landscape, vegetation and meteorological conditions have been operating since 1990's [6] including the AmeriFlux Eddy Covariance Flux Tower network [7] that are used in the present study. Measurements from these networks are generally available from the global FluxNet or AmeriFlux networks [8]. To simulate *ET*, process model input requirements vary from only temperature [9] to radiation [10] to a suite of meteorological, vegetation and soil parameters [11]. Additionally, these models generally estimate potential *ET* (*PET*) and must be combined with soil moisture models to limit *ET* based on moisture conditions (i.e., limited water availability) to determine actual *ET* [12–14].

Although significant research has been conducted on *ET*, much of the modeling focus has been on agricultural applications. For example, the Food and Agriculture Organization (FAO) of the United Nations has published an extensive document to determine crop water requirements based on an array of varying data availability [15]. Although the FAO methods can be applied as needed based on data availability, they do not provide global estimates of *ET*. For global estimates, gridded (i.e., 0.5–1.0 degree resolution) *ET* estimates from fully coupled water–energy balance hydrologic models operating at 3-h to monthly temporal resolutions are freely available from NASA'S Global Land Data Assimilation System (GLDAS) [16] or the National Center for Atmospheric Research's (NCAR) Community Earth System Model (CESM) [17]. There is also the relatively new MODIS (Moderate Resolution Imaging Spectroradiometer) *ET* product, MOD16, which provides *ET* estimates based on the Penman–Monteith (PM) method using a combination of remotely sensed vegetation measurements and re-analysis derived meteorological inputs [18,19].

Although it is possible to use *ET* (e.g., estimated from GLDAS or the MODIS *ET* product) as an independent time series for hydrologic study or as input to hydrologic models focused on event rainfall-runoff dynamics, there are two main challenges: limited ability to couple soil moisture-*ET* process models, which can impact model calibration, and the application of future climate conditions (e.g., IPCC AR5) for which the above *ET* estimates are not available due to lack of land surface vegetation characteristics in global scale climate models. The drawback with simulating *ET* processes within a hydrologic model is the uncertainty resulting from the number of required input parameters for determining available energy, meteorological conditions (humidity, vapor pressure deficit, wind speed, etc.) and resistance terms controlling water transfer. Models that use simulated soil moisture to alter *ET* resistance terms introduce additional parameter requirements and uncertainties [12]. Additionally, most of the *ET* products are not available on a daily scale, which is needed for hydrological modeling applications. For example, MODIS *ET* product is only available at 8-day, monthly, and annual scales [19]. However, there are some uncertainties and limitations associated with MODIS *ET* in different land cover types. For example, Liu, et al. [20] investigated eight sites from ChinaFLUX and showed MODIS *ET* performs better in grasslands as compared to croplands and evergreen forests with a general over-estimation of 6 mm/8-day and *RMSE* of 11 mm/8-day, where *ET* errors were linked to *LAI* estimation errors. Bhattarai, et al. [21] reported that MODIS *ET* under-estimated *ET* by 26% as evaluated at 13 AmeriFlux sites inside the United States; with site *RMSE* ranging from 8.5 to 9.4 mm/8-day. They linked their *ET* errors to the heterogeneity associated with each MODIS Land Surface Temperature (*LST*) pixel and the mismatch in spatial scales between MODIS products and ground based measurements. Velpuri, et al. [22] investigated MODIS *ET* estimations over 58 AmeriFlux sites and reported up to 25% uncertainty in MODIS *ET* product, suggesting the need for algorithm parameters refinement in the MOD16 product. Long, et al. [23] reported 10–15 mm/month uncertainty in MODIS *ET* over 3 regions in south central United States, relating the errors to energy and water balance constraints.

While the PM equation (e.g., used in MODIS *ET*) and associated forcing and parameter estimation methods typically reference air temperature (i.e., temperature measured under shelter at 2 m above the surface [24]), air temperature measurements are available at relatively few meteorological stations around the world providing limited data to capture relevant spatial patterns [24]. However, MODIS *LST* provides global surface temperatures, with no use of reanalysis data, providing consistent information, especially over places where there are either no or very few meteorological stations available. Thus, a central theme of this study is the applicability of MODIS *LST* for estimating global *ET* based on the PM equation.

There has been extensive research on the applicability of the MODIS *LST*. Benali, et al. [24] investigated the accuracy of MODIS *LST* over 106 meteorological stations in Portugal for a 10 year period and concluded that errors generally fall within 2 to 3 °C. Wan [25] reported that, in clear sky conditions where *LST* ranges from –10 °C to 58 °C, the accuracy of daily MODIS *LST* version 5 (V5) is better than 1 °C as compared to the in-situ measurements for most places and the *RMSE* is less than

0.5 °C for all places except for those with apparently heavy aerosol loadings. However, Wang, et al. [26] reported an under-estimation of 2–3 °C during nighttime for daily MODIS *LST* V4. Zhu, et al. [27] also reported *RMSEs* of 7.45 °C and 2.97 °C for daytime and nighttime daily *LST*, respectively, obtained from the Terra satellite and 9.44 °C and 4.41 °C obtained from Aqua satellite, over the Xiangride River basin in the north Tibetan Plateau during 2009 and 2010. Vancutsem, et al. [28] showed that nighttime MODIS *LST* provides good nighttime temperatures over different ecosystems in Africa, whereas, daytime estimations strongly vary with seasonality, ecosystems, solar radiation and cloud cover. Lin, et al. [29] reported disagreement of MODIS *LST* estimations and daily measurements in East Africa during the day ($MAE = 6.9 \pm 5$ °C), while suggesting better agreement during the night ($MAE = 1.9 \pm 1.7$ °C). Overall, the accuracy of MODIS *LST* varies from day to night, seasonally, with land cover, with cloud cover and aerosol loading [25].

Building on MODIS *ET* concepts, a globally applicable approach using MODIS *LST* for estimating daily *ET* is presented and compared to the MOD16 *ET* product and *ET* observations at 39 AmeriFlux sites. The novel aspect of this approach is the use of only remotely sensed measurements (i.e., no use of meteorological data, re-analysis data or in-situ measurements). For example, MOD16 *ET* uses derived meteorological inputs (humidity, air temperature, radiation) from NASA's Global Modeling and Assimilation Office (GMAO, v4.0.0) re-analysis dataset [19]. Here, the MODIS *ET* approach [18,19,30] is combined with FAO limited data methods for estimating vapor pressure and radiation [31] reducing meteorological input requirements to only temperature and vegetation characteristics, where both quantities are derived from MODIS products. This approach is taken to provide *ET* for use in large scale hydrologic models (i.e., as *ET* input or assessment) derived only from remotely sensed measurements (i.e., for regions without in-situ data) and to enable the prediction of future *ET* using coarse resolution future climate projections produced by Global Climate Models (GCMs). In this study, daily and monthly MODIS *LST* [25,32] are used and described in Table 1. However, the approach is applicable to any temperature series (e.g., daily or monthly climate model forecasts). For applications using future climate projections, spatial land cover and seasonal vegetation patterns and dynamics must be known or approximated based on current conditions.

Table 1. Descriptions of key datasets used in this study.

Quantity	MODIS ID	Temporal Resolution	Spatial Resolution	Reference
<i>ET</i>	MOD16	Daily, 8-day, and Monthly	30 s	[33]
Land Surface Temperature (<i>LST</i>)	MOD11C1 MOD11C3 MYD11C1 MYD11C3	Daily and monthly	0.05 degrees	[32]
Leaf Area Index (<i>LAI</i>)	MCD15A2	8-day composite	1 km	[34,35]
<i>FPAR</i>	MCD15A2	8-day composite	1 km	[34]
Albedo (α)	MCD43C3	16-day composite	0.05 degrees	[36]
Aerosol Optical Depth (<i>AOD</i>)	MOD08 MYD08	Monthly	1 degree	[37,38]
Land Cover (<i>LC</i>)	MCD12C1	Annual	0.05 degrees	[39]
Digital Elevation Model (<i>DEM</i>)	n/a	n/a	0.05 degrees	[40]
Wind Speed (<i>u</i>)	n/a	Mean Monthly	1 degree	[41]

2. Materials and Methods

Central to this study is the Penman–Monteith (PM) method for estimating *ET* (mm d^{-1}) based on the combination of energy and mass transfer concepts [11,15,30,42]:

$$\lambda ET = \frac{\Delta(R_n - G) + \frac{86,400\rho_a C_p(e_s - e_a)}{r_a}}{\Delta + \gamma\left(1 + \frac{r_s}{r_a}\right)} \quad (1)$$

where λ (MJ kg^{-1}) is the latent heat of vaporization; Δ ($\text{kPa } ^\circ\text{C}^{-1}$) is the slope of the saturation vapor pressure–temperature; R_n ($\text{MJ m}^2 \text{ day}^{-1}$) is net radiation; G ($\text{MJ m}^2 \text{ day}^{-1}$) is the soil heat flux; 86,400 is a unit conversion factor; ρ_a (kg m^{-3}) is the density of moist air density; C_p ($\text{MJ kg}^{-1} \text{ } ^\circ\text{C}^{-1}$) is the specific heat capacity of air; e_s and e_a (kPa) are saturated and actual vapor pressure, respectively; γ ($\text{kPa } ^\circ\text{C}^{-1}$) is the psychrometric constant; r_s (s m^{-1}) is water vaporization resistance from plants, soil or water surfaces; and r_a (s m^{-1}) is aerodynamic resistance. Here, λ , Δ , ρ_a , γ , e_s and e_a are a function of temperature and/or pressure, with pressure being a function of elevation. The resistance terms (r_s & r_a) are largely based on Vegetation Type and LAI [33]. For R_n , the FAO energy method [15] is used, which results in R_n at a given location being influenced only by latitude, Julian day, albedo (α), cloudiness, temperature (T_{min} , T_{mean} , T_{max}) and elevation (z). The soil heat flux is a minor component in the energy budget (often less than 5%) at daily and coarser scales [43]. Given our focus on daily ET , and the soil heat flux is neglected herein.

2.1. Datasets

The datasets in Table 1 are used to determine elevation, temperature, albedo as needed to solve the PM equation. Specific details are discussed below. Temperature forcings used in this study are based on four different MODIS derived LST measurements from NASA's Aqua and Terra satellites at roughly 1:30 a.m., 10:30 a.m., 1:30 p.m. and 10:30 p.m. (solar local times) [44]. Although the actual acquisition times vary over time, which likely influences the derived temperatures from the two satellites, the MODIS data products for day/night LST are used throughout the studied period. From the four measurements (i.e., day/night from Aqua/Terra), minimum and maximum values are determined, and the mean temperature is determined by averaging the minimum and maximum values. Note, the mean is based on averaging the two temperatures rather than the four to provide consistency for when measurements are available from only one satellite (i.e., two per day or month). Also note that, the level 3 MODIS LST data are used, which masks out bad data due to cloudiness or other reasons. Therefore, our analysis is only based on reliable data with no fill values for the missing days. Thus there is no ET estimation for days with no LST data.

Mean monthly wind speed at 50 m above the surface is used from NASA's Surface Meteorology and Solar Energy (SSE) data product; release 5 dataset (January 2005) consisting of 10-year monthly average (July 1983–June 1993). Wind speed at 50 m is converted to wind speed at 2 m above the surface (based on a method used by Allen, et al. [15]) and only used for estimating open water evaporation.

The datasets are obtained based on their product resolution listed in Table 1. In order to deal with different spatial resolutions, all datasets not gridded with 0.05 degree by 0.05 degree pixels, were either resampled to 0.05 degrees (e.g., Aerosol Optical Depth 1.0 degrees to 0.05 degrees) or upscaled to 0.05 degrees (e.g., LAI 1 km to 0.05 degrees). For resampling, all 0.05 degree pixels within the coarse resolution pixel were assigned the same value as the coarse resolution pixel. For upscaling, all finer resolution pixels within the 0.05 degree resolution pixel were averaged and the mean value was assigned to the 0.05 degree resolution pixel. For temporal resolution, the model was run daily and used the corresponding 8-day or monthly or annual products for each day.

2.2. Radiation

Net radiation (R_n) is the difference between the net shortwave radiation (R_{ns}) and the net longwave radiation (R_{nl}), where R_{ns} is the fraction of solar shortwave radiation (R_s) not reflected based on surface albedo (α): $R_{ns} = (1 - \alpha)R_s$. Albedo is estimated from black-sky, direct beam, albedo (BSA) and white-sky, completely diffuse, albedo (WSA) based on the fraction of diffuse skylight, $S(\theta, AOD)$, which is a function of solar zenith angle (θ) and Aerosol Optical Depth (AOD) [45]:

$$\alpha = \frac{S(\theta, AOD) WSA + (1 - S(\theta, AOD)) BSA}{1000} \quad (2)$$

The solar shortwave radiation is determined by:

$$R_s = 0.16 \sqrt{T_{max} - T_{min}} \times R_a \quad (3)$$

which uses the daily temperature range to account for cloudiness without using any cloudiness data [31,46,47], where R_a ($\text{MJ m}^2 \text{ day}^{-1}$) is the solar radiation above the atmosphere (extraterrestrial radiation), which is a function of the latitude, Julian day, and solar time (i.e., solar hour angle) [31]. R_{nl} is determined by:

$$R_{nl} = \sigma \left(\frac{(T_{max} + 273.15)^4 + (T_{min} + 273.15)^4}{2} \right) (0.34 - 0.14 \sqrt{e_a}) \left(1.35 \frac{R_s}{R_{s0}} - 0.35 \right) \quad (4)$$

where σ is the Stefan–Boltzmann constant ($4.903 \times 10^{-9} \text{ MJ K}^{-4} \text{ m}^{-2} \cdot \text{day}^{-1}$) and R_{s0} is the clear-sky solar radiations ($\text{MJ m}^2 \text{ day}^{-1}$):

$$R_{s0} = (0.75 + 2 \times 10^{-5} \times z) \times R_a \quad (5)$$

2.3. New Surface Fraction (Wet/Dry and Vegetated/Non-Vegetated) Methods

There are different methods for estimating the resistance terms (r_s & r_a) in the PM equation depending on the *ET* components being considered. Here, four *ET* water fluxes are represented for a given land area (e.g., 0.05 by 0.05 degree pixel) based on the fraction of vegetated (F_c) or non-vegetated ($1 - F_c$) land surface and the fraction of wet (F_w) or dry ($1 - F_w$) land surface Table 2. Studies have shown each component can control *ET* in different climate conditions. For example Li, et al. [48] showed that the soil water availability in hot-dry seasons and *LAI* in rainy seasons control *ET*. The resistance terms for each *ET* component are estimated based on methods listed in Mu, et al. [19], where each vegetation type has pre-defined resistance terms. Table 3 lists the Biome properties look-up table used here. The values were first derived by Running, et al. [49], and then revised by Heinsch, et al. [50]. The values listed in Table 3 are updated (http://files.ntsg.umt.edu/data/NTSG_Products/MOD16/readme) from values listed in Mu, et al. [19]. For land cover classified as open-water, evaporation is estimated based on Vallet-Coulomb, et al. [51] Table 2. Total *ET* for a given location (e.g., 0.05° grid cell) is the sum of all of *ET* components proportionally based on the location's land cover fractions. Note, land cover fractions are re-scaled to include only the largest three categories.

Table 2. Summary of *ET* component equations.

<i>ET</i> Components	Modifications to PM Equation *
Evaporation from Canopy	$E_c = F_c F_w ET(r_s, r_a)$
Transpiration from Vegetation	$E_t = F_c(1 - F_w) ET(r_s, r_a)$
Evaporation from Saturation Soil Surfaces	$E_{ss} = (1 - F_c) F_w ET(r_s, r_a)$
Evaporation from Moist Soil Surfaces	$E_s = (1 - F_c)(1 - F_w) ET(r_s, r_a) \left(\frac{RH}{100} \right)^{\frac{VPD}{200}}$
Evaporation from Open-Water	$E = \frac{\Delta(R_n - G)/\lambda + 2.6(1 + 0.54 \times u)(e_s - e_a)\gamma}{\Delta + \gamma}$ where u (m s^{-1}) is wind speed 2 m above surface [51].

* For canopy, vegetation and soil components, $ET(r_s, r_a)$ is determined using Equation (1) where the resistance terms vary based on the *ET* component following Mu, et al. [19] and Table 3.

Table 3. Biome specific parameter look-up table for Evergreen Needleleaf Forest (ENF), Evergreen Broadleaf Forest (EBF), Deciduous Needleleaf Forest (DNF), Deciduous Broadleaf Forest (DBF), Mixed Forest (MF), Closed Shrublands (CSH), Open Shrublands (OSH), Woody Savannas (WL), Savannas (SV), Grasslands (Grass), Croplands (Crop), Urban and Built-up (Urban), and Barren or Sparsely Vegetated (Barren); T_{min_open} , T_{min_close} , VPD_{open} , VPD_{close} determine boundary conditions for mT_{min} and $mVPD$ multipliers, which control transpiration, gl_sh and gl_e_wv are leaf conductance terms and Cl is a stomatal conductance term, RBL_{min} and RBL_{max} are boundary conditions that control soil resistance terms. See Mu, et al. [19] for more details. Light extinction coefficient (k) will be explained later.

LC	ENF	EBF	DNF	DBF	MF	CSH	OSH	WL	SV	Grass	Crop	Urban	Barren
T_{min_open} (°C)	8.31	9.09	10.44	9.94	9.50	8.61	8.80	11.39	11.39	12.02	12.02	12.02	12.02
T_{min_close} (°C)	−8.00	−8.00	−8.00	−6.00	−7.00	−8.00	−8.00	−8.00	−8.00	−8.00	−8.00	−8.00	−8.00
VPD_{close} (Pa)	3000	4000	3500	2900	2900	4300	4400	3500	3600	4200	4500	4200	4200
VPD_{open} (Pa)	650	1000	650	650	650	650	650	650	650	650	650	650	650
gl_sh (m s ^{−1})	0.01	0.01	0.01	0.01	0.01	0.02	0.02	0.04	0.04	0.02	0.02	0.02	0.02
gl_e_wv (m s ^{−1})	0.01	0.01	0.01	0.01	0.01	0.02	0.02	0.04	0.04	0.02	0.02	0.02	0.02
Cl (m s ^{−1})	0.0024	0.0024	0.0024	0.0024	0.0024	0.0055	0.0055	0.0055	0.0055	0.0055	0.0055	0.0055	0.0055
RBL_{min} (s m ^{−1})	60	60	60	60	60	60	60	60	60	60	60	60	60
RBL_{max} (s m ^{−1})	95	95	95	95	95	95	95	95	95	95	95	95	95
k	0.613	0.464	0.668	0.599	0.617	0.552	0.64	0.485	0.489	0.594	0.587	0.601	0.596

To estimate the four ET components explained in Table 2 for land pixels, F_c and F_w need to be determined. Here, the wet fraction (F_w) is based on humidity, and the vegetated fraction (F_c) is based on LAI . Each grid cell is divided into wet (F_w) and dry ($1 - F_w$) fractions. It is important to note that these fraction terms represent indexes used to determine the resistance terms that should be used in Equation (1). Building on Fisher, et al. [52], Mu, et al. [19] used the following equation to determine F_w .

$$F_w = \begin{cases} 0 & RH < 70\% \\ RH^4 & 70\% \leq RH \leq 100\% \end{cases} \quad (6)$$

saturated vapor pressure at T_{min} [53–55], and RH is calculated by:

$$RH = \frac{e_{s,Tmin}}{(e_{s,Tmin} + e_{s,Tmax})/2} \times 100 \quad (7)$$

where $e_{s,Tmin}$ and $e_{s,Tmax}$ (kPa) are the saturated vapor pressures at T_{min} and T_{max} , respectively, and determined using:

$$e_s = 0.6108 \times e^{\left(\frac{17.27T}{T+237.3}\right)} \quad (8)$$

Mu, et al. [19] F_w estimation method suggests a step at relative humidity of 70%. For some cases, this can create a large jump in ET (Figure 1), which is especially sensitive to temperature derived VPD and RH . As an alternative, we developed a revised approach (Equation (9)), based on the assumption of zero wet fraction for humidity conditions below a minimum threshold (RH_{min}) and a wet fraction of 1 for 100% humidity [52,56]. For humidity values from RH_{min} to 100%, the wet fraction varies from 0 to 1 as a linear or nonlinear function depending on the value of the exponent (β).

$$F_w = \begin{cases} 0 & RH < RH_{min} \\ \left(\frac{RH - RH_{min}}{1 - RH_{min}}\right)^\beta & RH_{min} \leq RH \leq 100\% \end{cases} \quad (9)$$

Values of RH_{min} and β are determined by minimizing the AmeriFlux sites meteorological data driven ET estimate (ET_{met}) errors at AmeriFlux sites for the period 2000–2006.

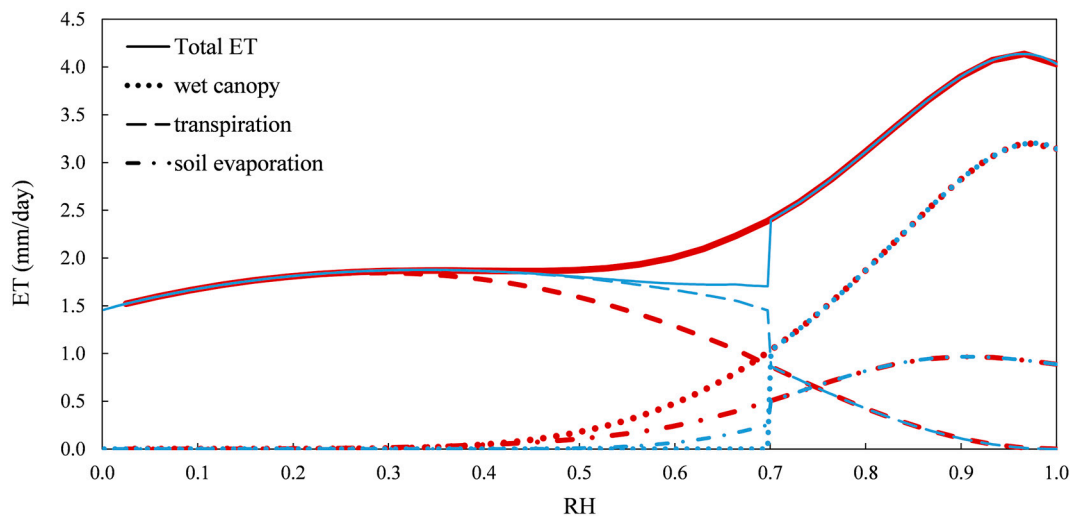


Figure 1. Variations in total and individual *ET* components as a function of relative humidity for select conditions (minimum and maximum temperatures of 15 °C and 30 °C, *LAI* of 4, albedo of 0.19, sea level elevation, 30 degrees latitude, EBF land cover type and time of year is mid-July): MODIS *ET* wet fraction method (Blue color), and wet fraction determined using Equation (9) with an β of 4 and RH_{min} of 0 (Red color).

Similar to surface wetness, each grid cell is divided into vegetated (F_c) and non-vegetated ($1 - F_c$) fractions. In previous studies, fractionation has been determined using Normalized or Enhanced Vegetation Indices products (*NDVI*, *EVI*) [18] or by using the Fraction of Photosynthetic Active Radiation (*FPAR*) [19]. To reduce the input data requirements (e.g., MODIS *FPAR* or *EVI/NDVI* products as in Mu, et al. [18] and Mu, et al. [19]) and capitalize on the strong correlation between *LAI* and *FPAR* [57–59], relationships between *LAI* and *FPAR* for each vegetation type [19,60] are developed to approximate F_c . A regression analysis based on a simplified model from the Beer–Lambert law for describing the light transition through various vegetation types [61–63] is used to estimate F_c :

$$F_c = FPAR = 0.95 \left(1 - e^{-k \times LAI} \right) \quad (10)$$

where the light extinction coefficient (k) can substantially vary for different land covers [64]. For example, k ranges from 0.4 to 0.7 for needleleaf forests and 0.5 to 0.8 for broadleaf forests. Aubin, et al. [65] reported a general value of 0.54 for all vegetation types and varying values of 0.37 to 0.98 for different vegetation types. In the present study, vegetation types are determined from MODIS Land Cover (MCD12C1; see Figure 2) and combined with MODIS *FPAR* (MCD12C1) and *LAI* (MCD15A2) to determine light extinction coefficients for each land cover type.

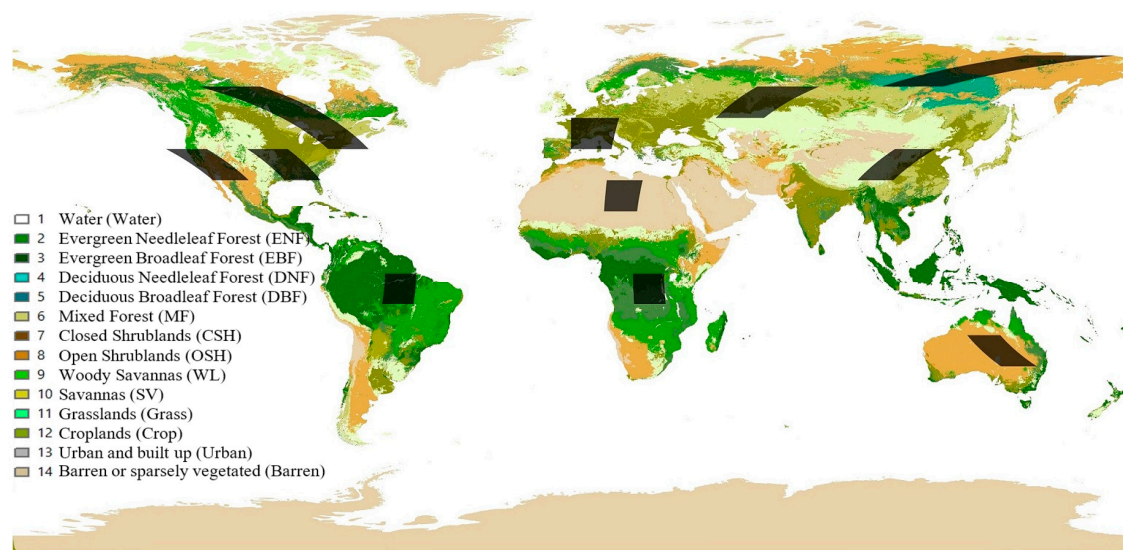


Figure 2. 2001 Land Cover (MCD12C1) with shaded squares showing the selected *FPAR/LAI* tiles used in this study.

2.4. Sheltering Factor

Although transpiration should decrease under water or temperature induced stress, these processes can be difficult to account for without simulating soil moisture or in-situ measurements. Here, temperature and *VPD* are used to reduce the potential stomatal conductance in cases of low humidity or cold temperatures to inhibit photosynthesis via mT_{min} and $mVPD$ multipliers [18,19]. However, under some specific conditions (e.g., highly vegetated locations where daily temperature gradients are roughly 10 °C or larger) simulated transpiration results in *ET* estimates exceeding Priestley–Taylor potential *ET* (*PT ET*) (Figure 3). While these conditions may be real, the use of temperature gradient to estimate *VPD* results in very low humidity, which is not realistic given the large fraction of vegetation. The high daily temperature gradient leads to high *VPD*, which both decrease the vegetation resistance to transpiration and increase the mass transfer flux. Such conditions provide great potential for transpiration, which especially takes place with introducing a high vegetation density to the model. Figure 3 shows such conditions for which transpiration estimation goes up almost monotonically with *LAI* leading to high *ET*. To overcome this challenge, we build on the Dingman [66] approach related to sheltering. Dingman [66] discussed that some leaves transpire at lower rates because they are “sheltered” from the sun and wind and defined a shelter factor (f_s) to account for this process. This factor decreases from 1 (open canopy) to 0.5 (closed canopy) as *LAI* increases [67,68]. Based on the mentioned studies, Jang, et al. [69] suggested the below constrain as a third multiplier (i.e., in addition to *VPD* and T_{min} controls) for canopy conductance:

$$f_s = \begin{cases} 1 - \frac{LAI}{6} & 0 \leq LAI < 3 \\ 0.5 & LAI \geq 3 \end{cases} \quad (11)$$

Here, the stomatal conductance is multiplied by the shelter factor (f_s) in addition to factors for *VPD* and T_{min} to further reduce conductance. As is shown in Figure 3, this factor decreases transpiration estimations. However, for the specific conditions represented in Figure 3, the reduced *ET* still exceeds potential *PT ET* as *LAI* increases above 4.6. Thus, additional research is needed to better understand the sheltering effect on transpiration.

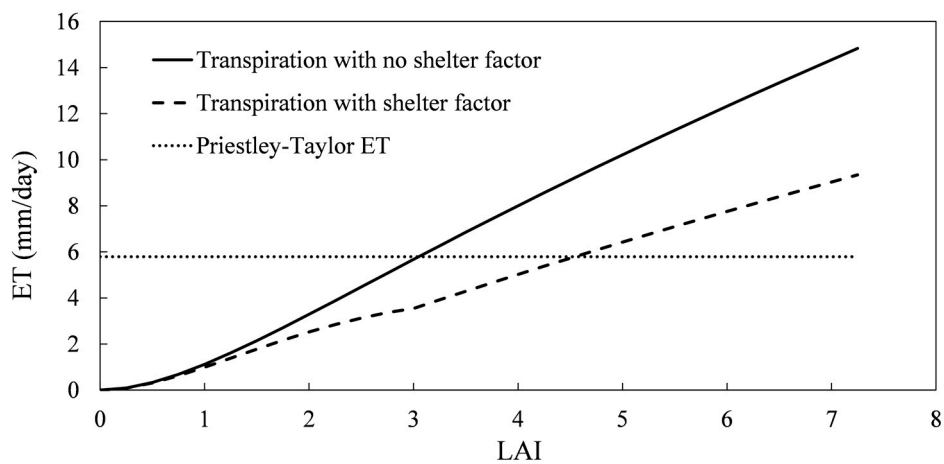


Figure 3. Variations in total ET with LAI with and without the shelter factor (f_s) to limit transpiration component of ET for a select location along with potential Priestley–Taylor ET (30 degrees latitude, 100 m elevation, closed shrublands land cover, albedo of 0.19, daily minimum maximum temperatures of 15 °C and 30 °C, time of year is mid-July).

2.5. Evaluation Method

The above methods enable ET to be estimated globally at daily temporal resolutions with a spatial resolution of 0.05 degrees. To evaluate simulated ET (ET_{LST}), in-situ measurements from the AmeriFlux network are used (ET_{obs}). In order to be consistent with the evaluation approach presented by Mu, et al. [19,39] AmeriFlux tower sites (Figure 4) with consistent vegetation types reported between the flux network and MOD12 land cover type 2, and measurements for more than half a year during 2000–2006 are used [19]. Following Mu, et al. [19] methods, these in-situ daily measurements are determined based on the Level 4 data consisting of half hour air temperature, VPD , incoming global solar radiation (shortwave radiation, 0.15–4.0 μm waveband including both direct radiation and diffuse radiation), and the latent heat flux (LE) at canopy level. To determine daily averages, only days containing 40 or more half hour measurements with quality control flags of “most reliable” were used with no daily fill values. However, note that the number of days at each site reported by Mu, et al. [19] is different than what is used in this study. This might be because the AmeriFlux network now provides more data at some sites and unlike the above study no fill value is used in the present study.

Note that, there is a mismatch in spatial resolution between tower measurements and simulated ET_{LST} . For example, tower data represent a footprint area, which varies with wind speed/direction and measurement heights, while remote sensing measurements and the resulting ET_{LST} estimates represent spatially averaged values over a sizeable landscape. Wang, et al. [70] assessed the representativeness of tower measurements and suggested that every eddy covariance tower footprints have an irregular spatial pattern similar to spatial distribution of prevailing wind direction and the flux sites with zonal vegetation has a better representativeness than site with non-zonal vegetation. Studies have suggested different up-scaling methods (e.g., [71]) to account for spatial mismatches. However, to provide error measures consistent with those reported for the MODIS ET product, the tower measurements (ET_{obs}) are compared to gridded ET_{LST} estimates directly [18,19]. Although the tower footprint areas (e.g., ~ 100 's m^2 to ~ 1 's km^2) are less than the simulated ET_{LST} pixel area ($\sim 25 \text{ km}^2$) and there are often energy balance closure problems associated with tower measurements [33,72,73], the tower-based estimates are applied uniformly over the pixel area. Thus, in this study, the flux tower measurements of ET_{obs} (i.e., LE/λ yielding ET_{obs} in units of mm/d for the associated footprint area) are compared directly to simulated ET_{LST} (i.e., ET_{LST} in mm/day for the pixel containing the tower location), for consistency with Mu, et al. [19]. Using the available measurements, three ET errors and two correlation-based terms are used to assess model performance:

$$\text{Bias} = \sum_{i=1}^n (M_i - O_i) \quad (12)$$

$$\text{Root Mean Square Error (RMSE)} = \sqrt{\frac{\sum_{i=1}^n (M_i - O_i)^2}{n}} \quad (13)$$

$$\text{Mean Absolute Error (MAE)} = \frac{\sum_{i=1}^n |M_i - O_i|}{n} \quad (14)$$

where M_i and O_i are, respectively, ET estimates and observations for day i , and n is the total number of days between 2000 and 2006 that have both ET observations and estimates at a particular AmeriFlux site. In addition, Correlation (R) and Taylor Skill Score (S) [74] are used:

$$S = \frac{4 \times (1 + R)}{\left(\frac{\sigma_M}{\sigma_O} + \frac{\sigma_O}{\sigma_M}\right)^2 \times (1 + R_0)} \quad (15)$$

where, σ_M and σ_O are the standard deviations in ET estimates and observations at a given site, and R_0 is the theoretical maximum correlation; assumed to be equal to one at all sites. Unlike $RMSE$ and MAE which can be impacted by the larger errors, R and S are more affected by trends/patterns. The range for R is -1 to 1 and S is 0 to 1 with higher values indicating better agreement between simulated and measured values for both. These four metrics are also used to provide consistency with previous MOD16 assessments [19].

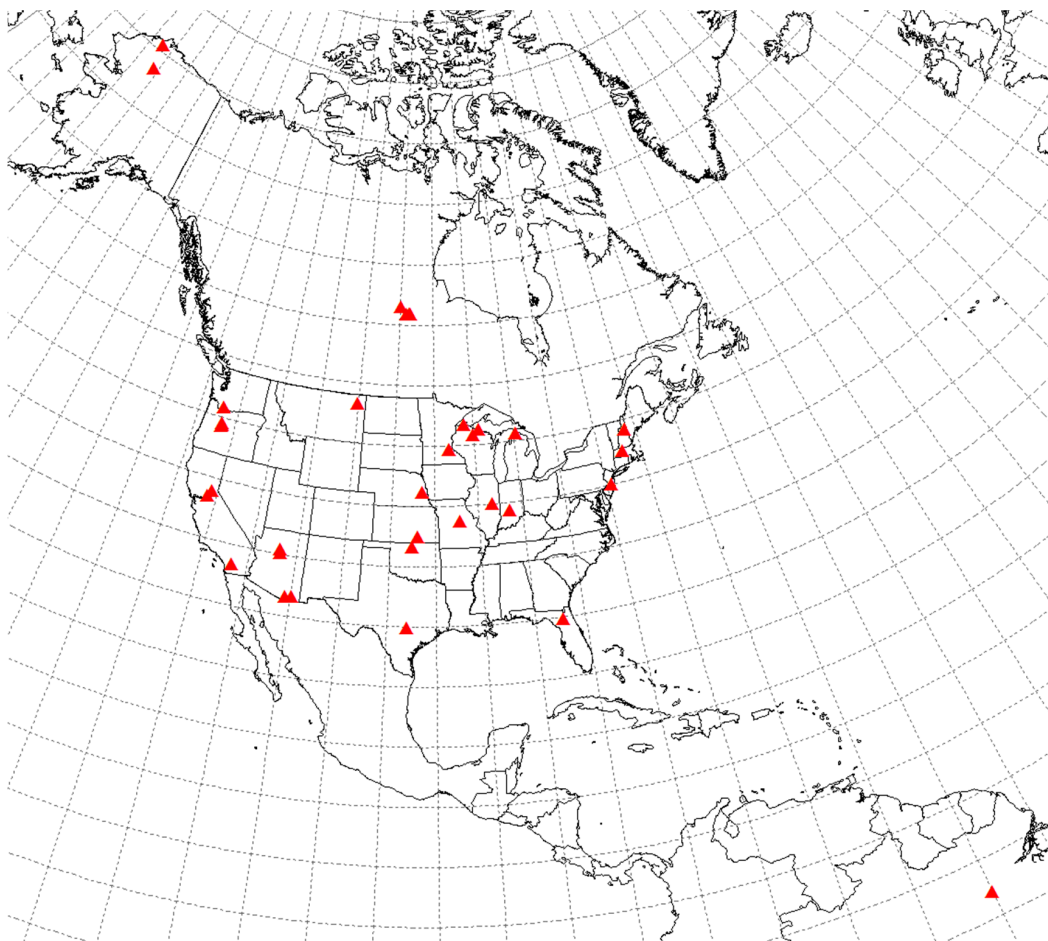


Figure 4. Locations of the AmeriFlux Eddy Covariance tower sites using in this study.

3. Results

3.1. Surface Fractions

First, results are presented for determining the wet and vegetated fractions. For F_w , values of RH_{min} and β in Equation (9) were optimized. The ET model was implemented with β values ranging from 1 to 10 stepping by 0.1 and RH_{min} values ranging from 0 to 1 stepping by 0.01. As shown in Figure 5a, the lowest $RMSE$ results from an RH_{min} of 0 and β of 4. Figure 5e shows the average AmeriFlux sites meteorological data driven ET_{met} for all sites with different RH_{min} and β values. The constant plain represents the average ET_{obs} value of 1.25 mm day^{-1} measured for all sites during the period of 2000–2006. The intersection of the average measurement and simulated surface is where the model matches the measurement mean. The resulting equation does not generate a step in the wet fraction and eliminates sudden changes in ET (Figure 1).

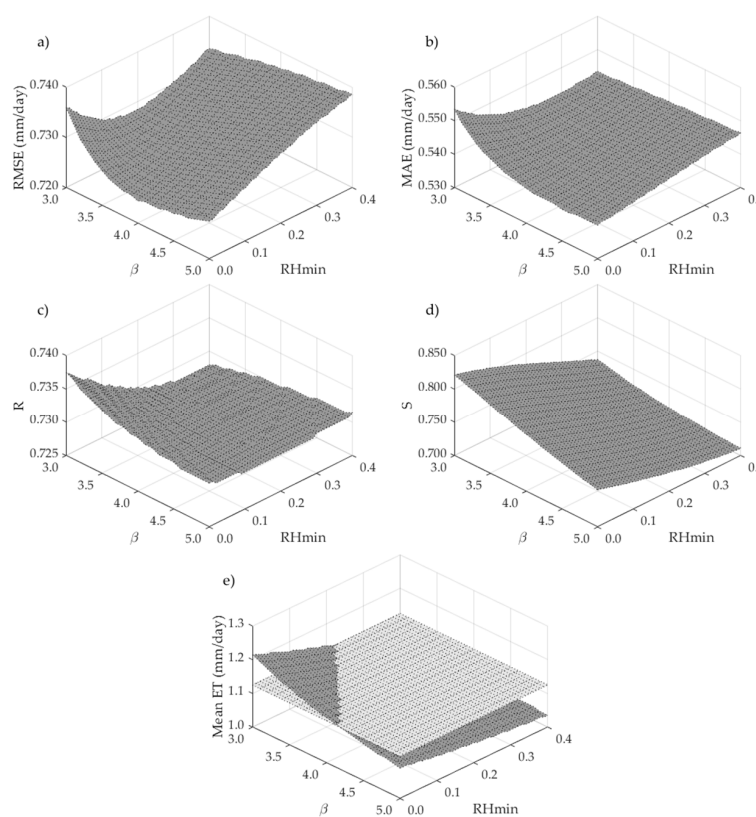


Figure 5. Relationships between mean error metrics (a–d) over the period of 2000–2006 from all study sites with the constants (RH_{min} and β) in Equation (4); (e) comparison between mean daily ET_{met} (shaded surface) and mean daily ET_{obs} (plain surface) over the period of 2000–2006 for all study sites.

To determine F_c using Equation (5), light extinction coefficients (k) for each LC type were determined. Twelve tiles from the MCD15A2 product were manually selected to capture representative vegetation regions distributed throughout the globe while ensuring all MODIS vegetation types were included for a large number of pixels. For sub-sampling within each tile, $FPAR$ and LAI values (from MCD15A2 product) from one thousand randomly selected points for each LC type were selected. To capture seasonal and annual variability, points were selected from: January, April, July, and October, in the years 2003, 2008 and 2013. Note that, the $FPAR/LAI$ correlation varies little from year to year. The main differences occur within a given year between the different seasons. For example, LAI increases dramatically during the spring growing season in North America. For each LC , k values were determined using all the selected points and Equation (5). To account for point selection uncertainty,

the above process was performed three separate times (i.e., different randomly selected points) and the final k values were determined by averaging the results from each scenario. Figure 6 shows the logarithmic relationship between LAI and $FPAR$ from a set of points extracted from the Evergreen Broadleaf Forest LC type (EBF). The slope of the line is the light extinction coefficient. Results for other LC 's are similar with a minimum R^2 value of 0.91. With k estimated, Figure 7 shows a comparison between LAI derived F_c using Equation (5) and $FPAR$ values for one MCD15A2 tile (h10v05) for all selected time periods. The k values based on the above analysis for all MODIS LC types (Table 3) range from 0.46 to 0.67 and are consistent to values reported in previous studies [64,65].

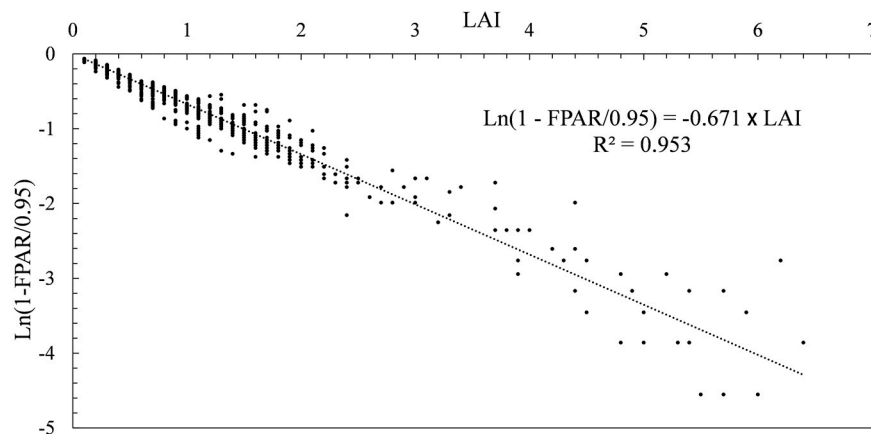


Figure 6. Relationship between LAI and $FPAR$ for points extracted from Evergreen Broadleaf Forests (EBF) land cover type, where the slope of the regression line represents the light extinction coefficient (k).

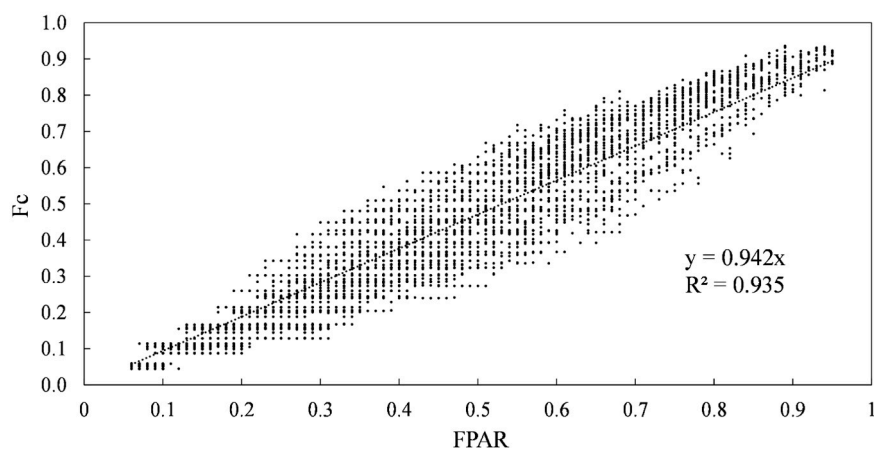


Figure 7. Comparison between LAI derived F_c values determined using Equation (5) and $FPAR$ values of a selected MCD15A2 tile (h10v05).

3.2. ET Estimations

Daily ET ($ET_{LST,d}$, $ET_{LST,m}$) based on daily or mean monthly LST , 16-day albedo, 8-day LAI and annual land cover was estimated for the period of 2000–2006. Note, when monthly temperatures are used, ET is still estimated daily using the same temperatures for each day of the month. In general, daily ET using monthly data is similar for 8-days based on the other MODIS values. However, there are slight 8-day changes in estimated shortwave radiation and LAI . Table 4 shows daily and monthly validations including minimum, maximum, median, and mean ET_{LST} with standard errors, average ET_{obs} and performance metrics over the 39 AmeriFlux sites used in this study (Figure 4). Note that the error measures are conducted based on daily estimates. The spatial resolution of ET_{LST} was 0.05 and 0.25 degrees, where all required input parameters were spatially averaged from their native

resolution to 0.05 or 0.25 degrees. Table 4 shows that our approach using MODIS LST results in an average bias of $-0.19 \text{ mm day}^{-1}$ ($ET_{LST,d}$) and $-0.09 \text{ mm day}^{-1}$ ($ET_{LST,m}$), $RMSE$ of 0.81 mm day^{-1} ($ET_{LST,d}$) and 0.77 mm day^{-1} ($ET_{LST,m}$), and MAE of 0.59 mm day^{-1} ($ET_{LST,d}$) and 0.56 mm day^{-1} ($ET_{LST,m}$). Correlations are 0.68 and 0.72 and Taylor Skill Scores are 0.74 and 0.7, for $ET_{LST,d}$ and $ET_{LST,m}$, respectively. Mu, et al. [19], who used meteorological re-analysis data, reported an average $RMSE$ of 0.87 mm day^{-1} , MAE of 0.27 mm day^{-1} , correlation of 0.56 and Taylor score of 0.54, over the same 39 sites. Here, $RMSE$, R and S metrics are improved but MAE is worse. However, it is important to note that numbers of days with available ET_{LST} estimates at each site are slightly different in this study as compared to those reported in Mu, et al. [19] as discussed above, which may also contribute to differences in performance measures. In addition, Mu, et al. [19] reported MAE values much lower than $RMSE$. For example, at a specific site (Tonzi Ranch), MAE is reported to be nearly perfect (0.01 mm day^{-1}) with a $RMSE$ of 0.67 mm day^{-1} . While the individual error measure seems reasonable, the ratio of MAE to $RMSE$ is not typical. For example, typical ratios of $MAE/RMSE$ is roughly 0.7 to 0.8 [75]. In this study, the ratio of mean $MAE/RMSE$ is 0.73 (for both $ET_{LST,d}$ and $ET_{LST,m}$), which is consistent with typically reported ratios.

Table 4. Summary of results and statistics at the AmeriFlux sites used in this study, where the min, max, median and mean values correspond to the mean ET (mm day^{-1}), $RMSE$ (mm day^{-1}), MAE (mm day^{-1}), R and S , based on daily ET estimates at each individual site using site measurements or MODIS datasets at a spatial resolution of 0.05 degrees; for MODIS derived values, mean ET_{LST} is the average of the daily means \pm the average of the standard error (se) of the daily means (discussed later) from each site. A supplementary table is provided showing the sites details.

		Observed Daily ET	Estimated Daily ET	$RMSE$	MAE	R	S
In-situ data driven results	min	0.44	0.44	0.42	0.30	0.33	0.47
	max	3.15	2.83	1.07	0.78	0.92	0.94
	median	1.06	1.12	0.71	0.52	0.82	0.83
	mean	1.25	1.23	0.69	0.51	0.76	0.80
MODIS data driven results (daily LST)	min	0.43	0.45	0.47	0.32	0.03	0.40
	max	3.28	2.68	1.33	1.01	0.88	0.91
	median	1.27	1.07	0.80	0.56	0.77	0.79
	mean \pm se	1.43	1.24 \pm 0.04	0.81	0.59	0.68	0.74
MODIS data driven results (monthly LST)	min	0.44	0.25	0.44	0.30	0.26	0.20
	max	3.15	2.82	1.17	0.90	0.86	0.91
	median	1.06	1.02	0.75	0.56	0.75	0.78
	mean \pm se	1.25	1.16 \pm 0.04	0.77	0.56	0.72	0.70

To assess the impacts of using temperature derived energy and VPD method, daily ET was simulated at each site using the in-situ metrological measurements described previously (ET_{met}). Overall, the mean ET_{met} from all sites for the period 2000–2006 is 1.23 mm day^{-1} using AmeriFlux tower input data, which is consistent with the mean of the ET_{obs} of 1.25 mm day^{-1} for the same sites and period (average bias = $-0.02 \text{ mm day}^{-1}$). Results show that $RMSE$ (0.69 mm day^{-1}), MAE (0.51 mm day^{-1}), R (0.76) and S (0.8) are all improved but remain similar in magnitude to ET_{LST} performance metrics. For comparison, $RMSE$, MAE , R and S are 0.82 mm day^{-1} , 0.30 mm day^{-1} , 0.62 and 0.56, respectively, in Mu, et al. [19]. Thus, the revised methods (i.e., not the meteorological inputs) used in this study compares reasonably to MOD16 methods, which uses more inputs. More importantly, the similar comparison between performance metrics for ET_{LST} and ET_{met} suggests that our methods using LST derived terms are reasonable.

To illustrate the variability of individual site/day performance, Figure 8 shows the comparison between daily ET_{LST} and ET_{obs} over the study period for all 39 AmeriFlux sites (Figure 4), where the 29,800 individual daily ET pairs are grouped by land cover type. The Figure shows that model

performance varies based on land cover. Although the large number of points represented in each plot make it difficult to assess mean performance, low ET_{LST} rates tend to be consistently overestimated at Evergreen Broadleaf Forest (EBF) sites (i.e., tropical rain forests) while the highest ET rates tend to be underestimated for Crops and Evergreen Needle Forest (ENF) site. However, for the majority of ET_{LST} ($<0.94 \text{ mm day}^{-1}$), estimates tend to mirror the 1:1 line with the exception of EBF. The range of variability along the 1:1 line also varies with land cover, with Woody Savannas (WL) sites have the greatest spread.

In terms of land cover and mean model performance, when using AmeriFlux site meteorological data, the model performs best for sites characterized as Evergreen Needleleaf Forests (ENF) with a mean bias of $-0.01 \text{ mm day}^{-1}$ and an average $RMSE$ of 0.58 mm day^{-1} , and worst for sites characterized as Evergreen Broadleaf Forests (EBF) with a mean bias of $-0.48 \text{ mm day}^{-1}$ and an average $RMSE$ of 0.78 mm day^{-1} . When using daily MODIS LST (Figure 8), the model performs best for ENF ($RMSE = 0.65 \text{ mm day}^{-1}$) and Savannas (SV) ($RMSE = 0.61 \text{ mm day}^{-1}$) but performs worst for Evergreen Broadleaf Forests (EBF) ($RMSE = 1.28 \text{ mm day}^{-1}$) and Croplands ($RMSE = 1.08 \text{ mm day}^{-1}$). In both cases, there is only a minimal change in model performance when using daily or mean monthly LST . The poor performance for EBF is consistent with the high LST errors that will be discussed later. The poor performance for cropland is likely due to transpiration resistance terms needing to be crop specific and the potential for soil moisture stress during the growing season.

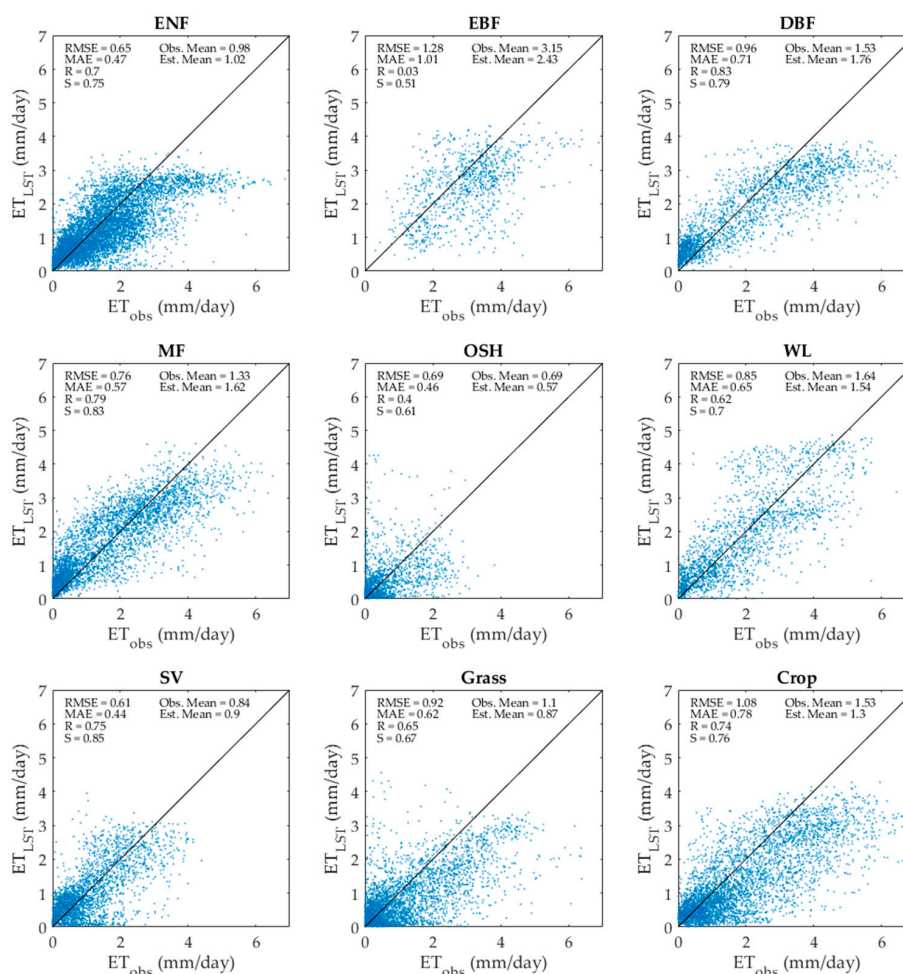


Figure 8. Comparison between daily ET_{obs} and ET_{LST} along with mean ET_{obs} and ET_{LST} and error measures for all the AmeriFlux sites used in this study over the period of 2000–2006 categorized into different land covers.

4. Discussion

4.1. Uncertainties in MODIS LST, LAI, Albedo and In-Situ Measurements

The model used in this study estimates daily ET without meteorological data such as humidity, radiation or cloud cover. Model forcings such as land cover (annual), albedo (16-day) and LAI (8-day) are assumed constant between measurements. The only input that varies daily is temperature. Building on the strong links between temperature and ET [76], temperature is used to determine net shortwave radiation (R_{ns}) by estimating cloud cover from the daily temperature range and is a key variable in calculating the net outgoing longwave radiation (R_{nl}). Additionally, temperature is used to estimate vegetation and soil resistance terms in the PM equation [19]. The primary role of temperature is in determining vapor pressure (humidity and VPD), which is used to determine the wet surface fraction.

We analyzed LST errors (for daily T_{min} and T_{max}) over 2000 to 2006 (i.e., the period investigated in this study) over all the sites and through different land covers. Other than Ever Green Broadleaf Forests (EBF), the correlation coefficients between remotely sensed temperature and in-situ measurements range from 0.85 to 0.92 for T_{min} and 0.82 to 0.95 for T_{max} . For EBF this value is 0.14 for T_{min} and 0.22 for T_{max} . Mean daily MODIS LST over the studied AmeriFlux sites is on average 0.3 °C lower than the measurements with an RMSE of 4.67 °C and MAE of 3.28 °C. Regardless of these challenges, MODIS LST provides global, consistent temperatures and is used herein. Additional discussion is provided below to highlight potential ET errors that likely results from day time LST uncertainty.

In addition to LST , MODIS LAI and Albedo products uncertainties are also included. Wang, et al. [77] indicated that RMSEs for the MCD43A Albedo product is less than 0.05 over grasslands, croplands and forests during dormant and snow-covered periods. Cescatti, et al. [78] found albedo MAEs of less than 0.02 over different land covers across the global FLUXNET network. For LAI , Yang, et al. [79] suggested a RMSE of 0.66 for the MODIS LAI product. Two recent studies [80,81] reported RMSE of 0.8 for the MCD15A2 V5 product, while Ganguly, et al. [82] suggests a RMSE of 0.5 LAI for different biomes.

To account for uncertainty in LST , LAI , Albedo and F_c in ET estimates, we build on the above studies to estimate uncertainties for each product. The ET algorithm is executed 100 times each time-step (daily over 2001–2013) for each pixel (globally), where values for LST , LAI , Albedo and estimated F_c are assigned a zero mean Gaussian random error with a standard deviation of 3 °C for LST , 0.7 for LAI , 0.05 for Albedo and ranging from 0.03 to 0.07 based on LC for F_c . For each time-step and each pixel the corresponding mean and standard deviation are determined [83]. The results of this analysis are provided in Table 4 as the mean \pm the standard error of the mean, averaged over the period of 2000–2006 for all AmeriFlux sites used in this study.

Another source of uncertainty is the in-situ measurements. Studies have suggested that ET measurements at Flux towers have errors of about 10–30% [19,84]. Also, the scale of our model (i.e., 0.05 or 0.25 degrees) is much coarser than the footprint of the eddy towers that have a horizontal scale of 2–5 m [18,19]. To overcome this discrepancy, especially at sites with heterogeneous environments, an upscaling process is recommended as a future work. Here, the uncertainty of the in-situ measurements is assumed to be much smaller in magnitude as compared to the remotely sensed measurements and not included in our analysis.

4.2. Sources of Errors in Estimations

Given our use of MODIS derived LST and VPD and their importance, it is likely that ET_{LST} errors are linked to LST and VPD errors, which is consistent with other studies [85,86]. For example, Figure 9 shows relationships between daily errors in T_{max} , VPD and ET_{LST} for AmeriFlux sites having grassland (Grass) and evergreen broadleaf forest (EBF) land cover types. As illustrated in Figure 9, our approach tends to under-estimate ET_{LST} for LC s with relatively low vegetation cover and low LAI (i.e., grasslands, croplands and savannas). In these locations, MODIS LST based T_{max} is often higher than the AmeriFlux site measurements, which leads to an over-estimation of VPD (Equation (3)).

In low LAI conditions, higher VPD results in lower surface wetness (i.e., smaller F_w) and increased water stress, which all leads to lower ET_{LST} . The lower ET_{LST} results from decreasing the fraction of high efficiency canopy evaporation from the fraction of saturated vegetation [$F_c F_w$] and decreasing transpiration from unsaturated vegetation [$F_c (1 - F_w)$] by increasing resistance. In contrast, this is often not the case for the forests that have relatively high vegetation density (high LAI) such as evergreen broadleaf forests (in Amazon), deciduous needleleaf forests, deciduous broadleaf forests, and mixed forests. For these LC s, over-estimation of VPD usually does not lead to an under-estimation of ET_{LST} because the surface wetness and soil moisture do not limit ET (i.e., Energy limited). Thus, higher VPD leads to higher ET . In other words, higher VPD or lower RH makes it easier for water flux to occur because there is less moisture in the air. This is consistent with the argument that in deciduous forests ET is generally energy limited and not water limited. In highly vegetated regions with high water availability, an over-estimation of VPD does not limit ET , and “actual” ET approaches “potential” ET .

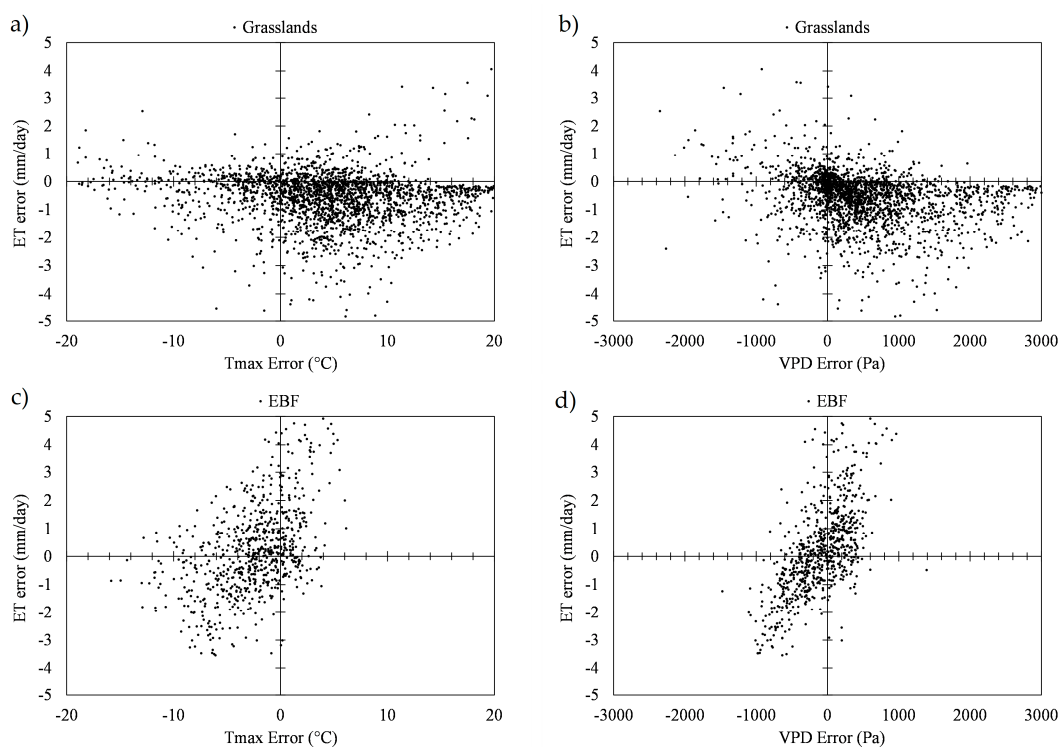


Figure 9. Days with different daily T_{max} (a,c) and VPD (b,d) errors versus ET_{LST} errors for grasslands (Grass) and Evergreen Broadleaf Forests (EBF) over the period of 2000–2006. Errors are daily estimates minus measurements.

Building on the above for Grasslands, it is more probable that an over (under) estimation of T_{max} or VPD leads to under (over) estimation of ET_{LST} . Thus, there is an “inverse” relationship between T_{max} and VPD errors with ET_{LST} error. In contrast, for the EBF LC type, there is a “direct” relationship. To further investigate the effects of vegetation density, relationships between the probability of VPD and ET_{LST} positive/negative errors and LAI were investigated. Figure 10 shows these relationships for the period 2000–2006 from sites representing different land covers. In general, the higher the LAI value the more probable the error relationships are direct, which is consistent with our above discussion. For example, when LAI is 4.5, 65% of the time in which VPD is over-estimated, ET_{LST} is also over-estimated, while for an LAI of 0.1 this occurs only 33% of the time (i.e., 67% of the time in which VPD is over-estimated, ET_{LST} is under-estimated). The key point of this discussion is that VPD error is likely a major contributor to ET_{LST} error.

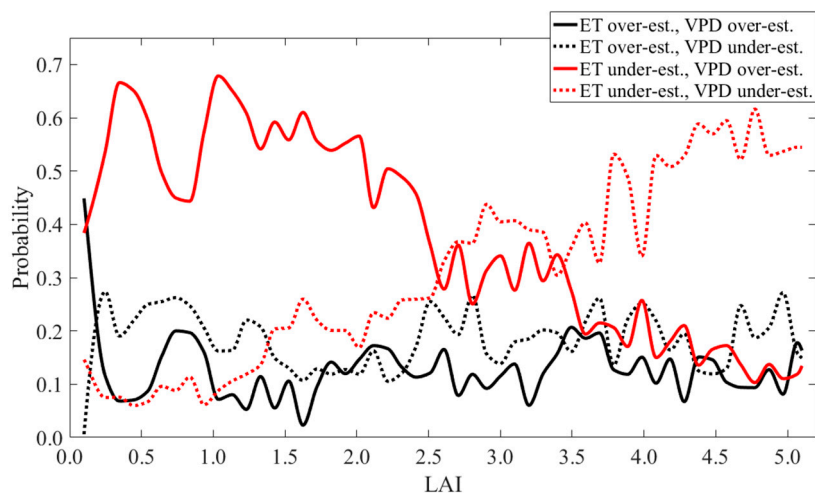


Figure 10. Probability of over- (black lines) or under-estimation (red lines) of ET_{LST} with corresponding over- (solid lines) or under-estimation (dashed lines) of VPD as a function of daily LAI at AmeriFlux sites; note, black solid and red dashed lines represent direct relationships between ET_{LST} and VPD errors while black dashed and red solid lines represent inverse relationships.

Another source of error is radiation. The method we use to account for cloudiness in estimating shortwave radiation (R_{ns}) links the LST errors to radiation (Equation (3)). As expected, our R_{ns} estimation method performs worst in EBF ($R = 0$) because of high LST errors in this land cover, while in other land covers it performs reasonably well with correlation coefficients range from 0.77 to 0.92.

4.3. Global Estimations

Monthly ET_{LST} is estimated globally (based on monthly MODIS LST grids, which have far less missing values than daily LST grids) for the period 2001–2013 both at 0.05 and 0.25 degree resolutions. Figure 11 shows mean monthly ET_{LST} corresponding standard errors and the difference between our approach and MOD16 ET product for the same period. In general, ET_{LST} is similar to MOD16 with an average difference of only 0.2 mm day⁻¹ less than MODIS ET (e.g., mean ET_{LST} for the near-global MODIS extent is 1.2 ± 0.2 mm day⁻¹ as compared to the mean MOD16 ET of 1.4 mm day⁻¹). Although the global patterns are similar, there are specific regions near the boundaries of the Congo and Amazon rainforests where ET_{LST} is much higher than MOD16 (e.g., 0.5–2.0 mm day⁻¹). These over-estimations generally result from transpiration over-estimations (i.e., regions on the boundary of tropical rainforests with high temperature ranges and considerable vegetation but lower rainfall than neighboring rainforests). Although the sheltering factor discussed previously, decreased transpiration over-estimations considerably, it cannot over-come the problem completely and future research is needed to resolve the problem (i.e., soil moisture stress function). In contrast, ET_{LST} is lower than MOD16 (e.g., 0.5–2 mm day⁻¹) in Amazon (i.e., Energy limited regions). Table 5 shows summary statistics for the ET_{LST} comparison based on LC types. Compared to MOD16, the largest difference occurs in the Evergreen Broadleaf Forests, where estimates are on average 0.97 mm day⁻¹ lower than MODIS. As discussed above, the problem in EBF is likely related to temperature ranges and resulting VPD , where lower VPD leads to lower ET_{LST} . In these regions, energy is typically the limiting factor and VPD should not limit ET_{LST} .

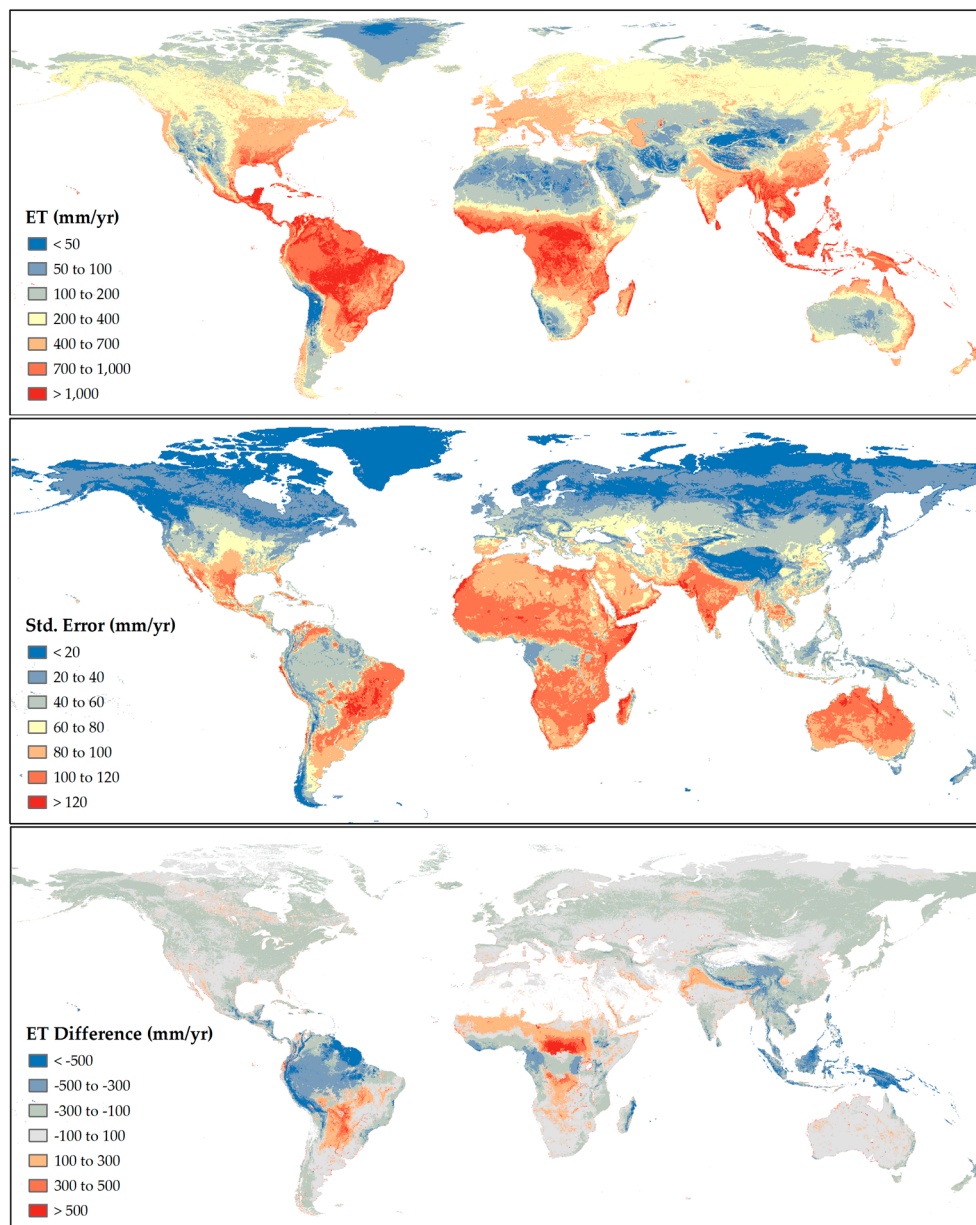


Figure 11. Mean annual ET_{LST} estimates over the period of 2001–2013 (**top**) and corresponding standard error estimates (**middle**), and difference between top and mean annual MODIS ET_{MOD16} [19] for the same period (**bottom**).

Although not shown here, the effects of spatial resolution were also investigated. ET_{LST} was estimated at both 0.05 and 0.25 degrees where all input datasets were spatially averaged to each respective resolution. Overall, there were minimal differences between results at the AmeriFlux sites based on 0.05 and 0.25 degree resolutions. The average $RMSE$ and MAE difference over the AmeriFlux sites between the two resolutions is less than 0.02 and 0.01 mm day^{-1} , respectively. The only noticeable differences were along shorelines where the coarse resolution included open water, which results into high ET_{LST} estimates.

Table 5. Summary statistics for the difference (mm day^{-1}) between ET_{LST} estimates and MODIS ET averaged over the period 2001–2013 based on 2001 land cover.

Land Cover	Min	Max	Range	Mean	Standard Deviation
ENF	−1.7	2.4	4.1	−0.20	0.17
EBF	−2.9	2.6	5.5	−0.97	0.49
DNF	−0.7	0.8	1.5	−0.36	0.10
DBF	−1.4	2.3	3.7	−0.14	0.50
MF	−2.1	2.7	4.8	−0.34	0.21
CSH	−2.6	1.7	4.3	0.03	0.35
OSH	−3.2	4.5	7.7	−0.16	0.24
WL	−2.4	2.8	5.2	−0.01	0.51
SV	−2.1	2.7	4.8	0.03	0.46
Grass	−3.2	3.7	6.9	−0.23	0.38
Crop	−2.4	3.8	6.2	−0.14	0.30
Urban	−2.9	3.6	6.5	−0.05	0.42
Barren	−3.8	5.0	8.8	−0.08	0.40

5. Conclusions

In this study, an approach was developed to simulate global ET using the Penman–Monteith equation and data products derived from only remotely sensed measurements (i.e., no in-situ or reanalysis datasets). Key components of the approach are new methods for estimating the fractions of vegetated and wet surfaces. New relationships are developed to estimate the vegetated fraction of the land areas based on LAI , MODIS land cover types and light extinction constants. A revised relationship for estimating the wet fraction of the land surface based on temperature-derived humidity is also presented.

Comparing ET performance metrics to those reported in Mu, et al. [19] suggests that the presented approach is comparable to MODIS ET while only using remotely sensed measurements. For example the presented approach results in an average $RMSE$ of 0.81 mm day^{-1} for ET_{LST} compared to a $RMSE$ of 0.87 mm day^{-1} reported by Mu, et al. [19] over the same AmeriFlux sites. When using the AmeriFlux meteorological datasets as inputs to the model, the presented approach results in an average $RMSE$ of 0.69 mm day^{-1} for ET_{met} compared to a $RMSE$ of 0.82 mm day^{-1} reported by Mu, et al. [19]. This study also highlights the importance of LST on ET estimates. For example, when maximum LST is over-estimated, our approach over-estimates VPD (i.e., lower humidity) resulting in cascading effects on mass transfer and wet surface contributions and resistance terms that impact ET estimates differently based on vegetation conditions. Over-estimates of maximum LST can lead to under-estimates of ET in sparsely vegetated areas (i.e., water limited regions) due to increased resistance controls, but over-estimates of ET in highly vegetated areas (i.e., energy limited regions) due to increased mass transfer contributions. Additional research is needed to reduce model sensitivity to over-estimations of maximum LST (i.e., humidity and VPD) in both water and energy limited conditions.

Supplementary Materials: The following are available online at www.mdpi.com/2072-4292/9/11/1138/s1. A supplementary table showing the AmeriFlux site details, model results and statistics for each site is provided.

Acknowledgments: This research was supported by NASA’s Terrestrial Hydrology (NNX12AQ36G, NNX14AD82G), GRACE (NNX12AJ95G) and SWOT (NNX16AQ39G) Programs. The authors acknowledge the data obtained from the MODIS products that were retrieved from the online data pool, courtesy of the NASA EOSDIS Land Processes Distributed Active Archive Center (LP DAAC), USGS/Earth Resources Observation and Science (EROS) Center, Sioux Falls, South Dakota. Also the authors acknowledge the wind data obtained from the NASA Langley Research Center Atmospheric Science Data Center Surface meteorological and Solar Energy (SSE) web portal supported by the NASA LaRC Prediction of Worldwide Energy Resource (POWER) Project. Additionally, the investigators acknowledge the data obtained from AmeriFlux data resources that was funded by the U.S. Department of Energy’s Office of Science.

Author Contributions: This manuscript is part of the PhD research work done at Northeastern University. Roozbeh Raoufi was the main author involved in data collection and analysis, and manuscript preparation. Edward Beighley played a supervisory role, editing and was involved in research project concept development.

Conflicts of Interest: The authors declare no conflict of interest. The funding sponsors had no role in the design of the study; in the collection, analyses, or interpretation of data; in the writing of the manuscript, and in the decision to publish the results.

References

1. Korzoun, V.; Sokolov, A.; Budyko, M.; Voskresensky, K.; Kalinin, G.; Konoplyantsev, A.; Korotkevich, E.; Kuzin, P.; Lvovich, M. *World Water Balance and Water Resources of the Earth*; Studies and Reports in Hydrology (UNESCO); UNESCO: Paris, France, 1978.
2. L'vovich, M.I.; White, G.F.; Belyaev, A.; Kindler, J.; Koronkevic, N.; Lee, T.R.; Voropaev, G. Use and transformation of terrestrial water systems. In *The Earth as Transformed by Human Action: Global and Regional Changes in the Biosphere over the Past*; Cambridge University Press: Cambridge, UK, 1990; Volume 300, pp. 235–252.
3. Li, H.; Wigmosta, M.S.; Wu, H.; Huang, M.; Ke, Y.; Coleman, A.M.; Leung, L.R. A physically based runoff routing model for land surface and earth system models. *J. Hydrometeorol.* **2013**, *14*, 808–828. [[CrossRef](#)]
4. Yamazaki, D.; Kanae, S.; Kim, H.; Oki, T. A physically based description of floodplain inundation dynamics in a global river routing model. *Water Resour. Res.* **2011**, *47*. [[CrossRef](#)]
5. Fleischer, E.; Bölter, J.; Klemm, O. Summer evapotranspiration in western Siberia: A comparison between eddy covariance and Penman method formulations. *Hydrol. Process.* **2015**, *29*, 4498–4513. [[CrossRef](#)]
6. Nagler, P. The role of remote sensing observations and models in hydrology: The science of evapotranspiration. *Hydrol. Process.* **2011**, *25*, 3977–3978. [[CrossRef](#)]
7. Baldocchi, D.; Valentini, R.; Running, S.; Oechel, W.; Dahlman, R. Strategies for measuring and modelling carbon dioxide and water vapour fluxes over terrestrial ecosystems. *Glob. Chang. Biol.* **1996**, *2*, 159–168. [[CrossRef](#)]
8. Baldocchi, D.; Falge, E.; Gu, L.; Olson, R. FLUXNET: A new tool to study the temporal and spatial variability of ecosystem-scale carbon dioxide, water vapor, and energy flux densities. *Bull. Am. Meteorol. Soc.* **2001**, *82*, 2415. [[CrossRef](#)]
9. Thornthwaite, C.W. An approach toward a rational classification of climate. *Geogr. Rev.* **1948**, *38*, 55–94. [[CrossRef](#)]
10. Priestley, C.; Taylor, R. On the assessment of surface heat flux and evaporation using large-scale parameters. *Mon. Weather Rev.* **1972**, *100*, 81–92. [[CrossRef](#)]
11. Monteith, J. Evaporation and environment. *Symp. Soc. Exp. Biol.* **1965**, *19*, 205–234. [[PubMed](#)]
12. Beighley, R.; Eggert, K.; Dunne, T.; He, Y.; Gummadi, V.; Verdin, K. Simulating hydrologic and hydraulic processes throughout the Amazon River Basin. *Hydrol. Process.* **2009**, *23*, 1221–1235. [[CrossRef](#)]
13. Hong, J.; Takagi, K.; Ohta, T.; Kodama, Y. Wet surface resistance of forest canopy in monsoon Asia: Implications for eddy-covariance measurement of evapotranspiration. *Hydrol. Process.* **2014**, *28*, 37–42. [[CrossRef](#)]
14. Senay, G.; Leake, S.; Nagler, P.; Artan, G.; Dickinson, J.; Cordova, J.; Glenn, E. Estimating basin scale evapotranspiration (ET) by water balance and remote sensing methods. *Hydrol. Process.* **2011**, *25*, 4037–4049. [[CrossRef](#)]
15. Allen, R.G.; Pereira, L.S.; Raes, D.; Smith, M. *Crop Evapotranspiration—Guidelines for Computing Crop Water Requirements—FAO Irrigation and Drainage Paper 56*; FAO: Rome, Italy, 1998; Volume 300, p. 6541.
16. Rodell, M.; Houser, P.R.; Jambor, U.; Gottschalck, J.; Mitchell, K.; Meng, C.J.; Arsenault, K.; Cosgrove, B.; Radakovich, J.; Bosilovich, M.; et al. The Global Land Data Assimilation System. *Bull. Am. Meteorol. Soc.* **2004**, *85*, 381–394. [[CrossRef](#)]
17. Kay, J.E.; Deser, C.; Phillips, A.; Mai, A.; Hannay, C.; Strand, G.; Arblaster, J.M.; Bates, S.C.; Danabasoglu, G.; Edwards, J.; et al. The Community Earth System Model (CESM) Large Ensemble Project: A Community Resource for Studying Climate Change in the Presence of Internal Climate Variability. *Bull. Am. Meteorol. Soc.* **2014**, *96*, 1333–1349. [[CrossRef](#)]
18. Mu, Q.; Heinsch, F.A.; Zhao, M.; Running, S.W. Development of a global evapotranspiration algorithm based on MODIS and global meteorology data. *Remote Sens. Environ.* **2007**, *111*, 519–536. [[CrossRef](#)]

19. Mu, Q.Z.; Zhao, M.S.; Running, S.W. Improvements to a MODIS global terrestrial evapotranspiration algorithm. *Remote Sens. Environ.* **2011**, *115*, 1781–1800. [[CrossRef](#)]
20. Liu, Z.; Shao, Q.; Liu, J. The performances of MODIS-GPP and-ET products in China and their sensitivity to input data (FPAR/LAI). *Remote Sens.* **2014**, *7*, 135–152. [[CrossRef](#)]
21. Bhattarai, N.; Mallick, K.; Brunsell, N.A.; Sun, G.; Jain, M. Regional evapotranspiration from image-based implementation of the Surface Temperature Initiated Closure (STIC1.2) model and its validation across an aridity gradient in the conterminous United States. *Hydrol. Earth Syst. Sci. Discuss.* **2017**, in review. [[CrossRef](#)]
22. Velpuri, N.M.; Senay, G.B.; Singh, R.K.; Bohms, S.; Verdin, J.P. A comprehensive evaluation of two MODIS evapotranspiration products over the conterminous United States: Using point and gridded FLUXNET and water balance ET. *Remote Sens. Environ.* **2013**, *139*, 35–49. [[CrossRef](#)]
23. Long, D.; Longuevergne, L.; Scanlon, B.R. Uncertainty in evapotranspiration from land surface modeling, remote sensing, and GRACE satellites. *Water Resour. Res.* **2014**, *50*, 1131–1151. [[CrossRef](#)]
24. Benali, A.; Carvalho, A.; Nunes, J.; Carvalhais, N.; Santos, A. Estimating air surface temperature in Portugal using MODIS LST data. *Remote Sens. Environ.* **2012**, *124*, 108–121. [[CrossRef](#)]
25. Wan, Z. New refinements and validation of the MODIS land-surface temperature/emissivity products. *Remote Sens. Environ.* **2008**, *112*, 59–74. [[CrossRef](#)]
26. Wang, W.; Liang, S.; Meyers, T. Validating MODIS land surface temperature products using long-term nighttime ground measurements. *Remote Sens. Environ.* **2008**, *112*, 623–635. [[CrossRef](#)]
27. Zhu, W.; Lú, A.; Jia, S. Estimation of daily maximum and minimum air temperature using MODIS land surface temperature products. *Remote Sens. Environ.* **2013**, *130*, 62–73. [[CrossRef](#)]
28. Vancutsem, C.; Ceccato, P.; Dinku, T.; Connor, S.J. Evaluation of MODIS land surface temperature data to estimate air temperature in different ecosystems over Africa. *Remote Sens. Environ.* **2010**, *114*, 449–465. [[CrossRef](#)]
29. Lin, S.; Moore, N.J.; Messina, J.P.; DeVisser, M.H.; Wu, J. Evaluation of estimating daily maximum and minimum air temperature with MODIS data in east Africa. *Int. J. Appl. Earth Obs. Geoinf.* **2012**, *18*, 128–140. [[CrossRef](#)]
30. Cleugh, H.A.; Leuning, R.; Mu, Q.; Running, S.W. Regional evaporation estimates from flux tower and MODIS satellite data. *Remote Sens. Environ.* **2007**, *106*, 285–304. [[CrossRef](#)]
31. Allen, R. *Evaluation of Procedures for Estimating Mean Monthly Solar Radiation from Air Temperature*; FAO: Rome, Italy, 1995.
32. Wan, Z. *MODIS Land-Surface Temperature Algorithm Theoretical Basis Document (LST ATBD)*; Institute for Computational Earth System Science: Santa Barbara, CA, USA, 1999; Volume 75.
33. Mu, Q.; Zhao, M.; Running, S.W. *MODIS Global Terrestrial Evapotranspiration (ET) Product (NASA MOD16A2/A3)*; Algorithm Theoretical Basis Document, Collection; Numerical Terradynamic Simulation Group: Missoula, MT, USA, 2013; Volume 5.
34. Knyazikhin, Y.; Glassy, J.; Privette, J.; Tian, Y.; Lotsch, A.; Zhang, Y.; Wang, Y.; Morisette, J.; Votava, P.; Myneni, R. *MODIS Leaf Area Index (LAI) and Fraction of Photosynthetically Active Radiation Absorbed by Vegetation (FPAR) Product (MOD15) Algorithm Theoretical Basis Document*; Theoretical Basis Document; NASA Goddard Space Flight Center: Greenbelt, MD, USA, 1999; Volume 20771.
35. Yuan, H.; Dai, Y.; Xiao, Z.; Ji, D.; Shangguan, W. Reprocessing the MODIS Leaf Area Index products for land surface and climate modelling. *Remote Sens. Environ.* **2011**, *115*, 1171–1187. [[CrossRef](#)]
36. Strahler, A.H.; Muller, J.; Lucht, W.; Schaaf, C.; Tsang, T.; Gao, F.; Li, X.; Lewis, P.; Barnsley, M.J. MODIS BRDF/albedo product: Algorithm theoretical basis document version 5.0. *MODIS Doc.* **1999**, *23*, 42–47. Available online: dratmos.geog.umd.edu/files/pdf/MODIS_BRDF.pdf (accessed on 3 November 2017).
37. Lewis, P.; Barnsley, M. Influence of the sky radiance distribution on various formulations of the earth surface albedo. In Proceedings of the 6th International Symposium on Physical Measurements and Signatures in Remote Sensing, ISPRS, CNES, Val d’Isere, France, 17–21 January 1994; pp. 707–715.
38. Lucht, W.; Schaaf, C.B.; Strahler, A.H. An algorithm for the retrieval of albedo from space using semiempirical BRDF models. *IEEE Trans. Geosci. Remote Sens.* **2000**, *38*, 977–998. [[CrossRef](#)]
39. Strahler, A.; Muchoney, D.; Borak, J.; Friedl, M.; Gopal, S.; Lambin, E.; Moody, A. MODIS Land Cover Product Algorithm Theoretical Basis Document (ATBD) Version 5.0. 1999. Available online: <https://pdfs.semanticscholar.org/8c83/49d66f9d663d7e7ccf9e0632edde719a1892.pdf> (accessed on 3 November 2017).

40. O'Callaghan, J.F.; Mark, D.M. The extraction of drainage networks from digital elevation data. *Comput. Vis. Graph. Image Process.* **1984**, *28*, 323–344. [[CrossRef](#)]
41. Stackhouse, P.; Whitlock, C. *Surface Meteorology and Solar Energy (SSE) Release 6.0 Methodology*, NASA SSE 6.0; Earth Science Enterprise Program; National Aeronautic and Space Administration(NASA): Langley, WA, USA, 2009.
42. Penman, H.L. Natural evaporation from open water, bare soil and grass. *Proc. R. Soc. Lond. Ser. A Math. Phys. Sci.* **1948**, *193*, 120–145. [[CrossRef](#)]
43. Running, S.W.; Kimball, J.S. Satellite-Based Analysis of Ecological Controls for Land-Surface Evaporation Resistance. In *Encyclopedia of Hydrological Sciences*; John Wiley & Sons, Ltd.: Hoboken, NJ, USA, 2005.
44. Wan, Z.; Zhang, Y.; Zhang, Q.; Li, Z.-L. Quality assessment and validation of the MODIS global land surface temperature. *Int. J. Remote Sens.* **2004**, *25*, 261–274. [[CrossRef](#)]
45. Schaaf, C.B.; Gao, F.; Strahler, A.H.; Lucht, W.; Li, X.; Tsang, T.; Strugnell, N.C.; Zhang, X.; Jin, Y.; Muller, J.-P. First operational BRDF, albedo nadir reflectance products from MODIS. *Remote Sens. Environ.* **2002**, *83*, 135–148. [[CrossRef](#)]
46. Hargreaves, G.H.; Samani, Z.A. Estimating potential evapotranspiration. *J. Irrig. Drain. Div.* **1982**, *108*, 225–230.
47. Richardson, C. Weather simulation for crop management models. *Trans. ASAE* **1985**, *28*, 1602–1606. [[CrossRef](#)]
48. Li, Z.; Zhang, Y.; Wang, S.; Yuan, G.; Yang, Y.; Cao, M. Evapotranspiration of a tropical rain forest in Xishuangbanna, southwest China. *Hydrol. Process.* **2010**, *24*, 2405–2416. [[CrossRef](#)]
49. Running, S.W.; Thornton, P.E.; Nemani, R.; Glassy, J.M. Global terrestrial gross and net primary productivity from the Earth Observing System. In *Methods in Ecosystem Science*; Springer: Berlin, Germany, 2000; pp. 44–57.
50. Heinsch, F.A.; Reeves, M.; Votava, P.; Kang, S.; Milesi, C.; Zhao, M.; Glassy, J.; Jolly, W.M.; Loehman, R.; Bowker, C.F. GPP and NPP (MOD17A2/A3) Products NASA MODIS Land Algorithm. *MOD17 User's Guide*. 2003. Available online: www.academia.edu/download/36531869/MOD17UsersGuide.pdf (accessed on 7 November 2017).
51. Vallet-Coulomb, C.; Legesse, D.; Gasse, F.; Travi, Y.; Chernet, T. Lake evaporation estimates in tropical Africa (Lake Ziway, Ethiopia). *J. Hydrol.* **2001**, *245*, 1–18. [[CrossRef](#)]
52. Fisher, J.B.; Tu, K.P.; Baldocchi, D.D. Global estimates of the land-atmosphere water flux based on monthly AVHRR and ISLSCP-II data, validated at 16 FLUXNET sites. *Remote Sens. Environ.* **2008**, *112*, 901–919. [[CrossRef](#)]
53. Glassy, J.M.; Running, S.W. Validating Diurnal Climatology Logic of the MT-CLIM Model Across a Climatic Gradient in Oregon. *Ecol. Appl.* **1994**, *4*, 248–257. [[CrossRef](#)]
54. Kimball, J.; Running, S.; Nemani, R. An improved method for estimating surface humidity from daily minimum temperature. *Agric. For. Meteorol.* **1997**, *85*, 87–98. [[CrossRef](#)]
55. Running, S.W.; Nemani, R.R.; Hungerford, R.D. Extrapolation of synoptic meteorological data in mountainous terrain and its use for simulating forest evapotranspiration and photosynthesis. *Can. J. For. Res.* **1987**, *17*, 472–483. [[CrossRef](#)]
56. Stone, P.; Chow, S.; Quirr, W. The July climate and a comparison of the January and July climates simulated by the GISS general circulation model. *Mon. Weather Rev.* **1977**, *105*, 170–194. [[CrossRef](#)]
57. Myneni, R.; Hoffman, S.; Knyazikhin, Y.; Privette, J.; Glassy, J.; Tian, Y.; Wang, Y.; Song, X.; Zhang, Y.; Smith, G. Global products of vegetation leaf area and fraction absorbed PAR from year one of MODIS data. *Remote Sens. Environ.* **2002**, *83*, 214–231. [[CrossRef](#)]
58. Wang, Q.; Adiku, S.; Tenhunen, J.; Granier, A. On the relationship of NDVI with leaf area index in a deciduous forest site. *Remote Sens. Environ.* **2005**, *94*, 244–255. [[CrossRef](#)]
59. Wang, Y.; Tian, Y.; Zhang, Y.; El-Saleous, N.; Knyazikhin, Y.; Vermote, E.; Myneni, R.B. Investigation of product accuracy as a function of input and model uncertainties: Case study with SeaWiFS and MODIS LAI/FPAR algorithm. *Remote Sens. Environ.* **2001**, *78*, 299–313. [[CrossRef](#)]
60. Los, S.; Pollack, N.; Parris, M.; Collatz, G.; Tucker, C.; Sellers, P.; Malmström, C.; DeFries, R.; Bounoua, L.; Dazlich, D. A global 9-year biophysical land surface dataset from NOAA AVHRR data. *J. Hydrometeorol.* **2000**, *1*, 183–199. [[CrossRef](#)]

61. Norman, J.M.; Kustas, W.P.; Humes, K.S. Source approach for estimating soil and vegetation energy fluxes in observations of directional radiometric surface temperature. *Agric. For. Meteorol.* **1995**, *77*, 263–293. [[CrossRef](#)]
62. Ruimy, A.; Kergoat, L.; Bondeau, A.; Intercomparison, T.; Model, P.O. Comparing global models of terrestrial net primary productivity (NPP): Analysis of differences in light absorption and light-use efficiency. *Glob. Chang. Biol.* **1999**, *5*, 56–64. [[CrossRef](#)]
63. Sellers, P.J.; Tucker, C.J.; Collatz, G.J.; Los, S.O.; Justice, C.O.; Dazlich, D.A.; Randall, D.A. A revised land surface parameterization (SiB2) for atmospheric GCMs. Part II: The generation of global fields of terrestrial biophysical parameters from satellite data. *J. Clim.* **1996**, *9*, 706–737. [[CrossRef](#)]
64. Jarvis, P.; Leverenz, J. Productivity of temperate, deciduous and evergreen forests. In *Physiological Plant Ecology IV*; Springer: Berlin, Germany, 1983; pp. 233–280.
65. Aubin, I.; Beaudet, M.; Messier, C. Light extinction coefficients specific to the understory vegetation of the southern boreal forest, Quebec. *Can. J. For. Res.* **2000**, *30*, 168–177. [[CrossRef](#)]
66. Dingman, S.L. *Physical Hydrology*; Waveland Press: Long Grove, IL, USA, 2015.
67. Allen, R.G.; Jensen, M.E.; Wright, J.L.; Burman, R.D. Operational estimates of reference evapotranspiration. *Agron. J.* **1989**, *81*, 650–662. [[CrossRef](#)]
68. Carlson, T.N. Modeling stomatal resistance: An overview of the 1989 workshop at the Pennsylvania State University. *Agric. For. Meteorol.* **1991**, *54*, 103–106. [[CrossRef](#)]
69. Jang, K.; Kang, S.; Kim, J.; Lee, C.B.; Kim, T.; Kim, J.; Hirata, R.; Saigusa, N. Mapping evapotranspiration using MODIS and MM5 four-dimensional data assimilation. *Remote Sens. Environ.* **2010**, *114*, 657–673. [[CrossRef](#)]
70. Wang, H.; Jia, G.; Zhang, A.; Miao, C. Assessment of Spatial Representativeness of Eddy Covariance Flux Data from Flux Tower to Regional Grid. *Remote Sens.* **2016**, *8*, 742. [[CrossRef](#)]
71. Liu, S.; Xu, Z.; Song, L.; Zhao, Q.; Ge, Y.; Xu, T.; Ma, Y.; Zhu, Z.; Jia, Z.; Zhang, F. Upscaling evapotranspiration measurements from multi-site to the satellite pixel scale over heterogeneous land surfaces. *Agric. For. Meteorol.* **2016**, *230*, 97–113. [[CrossRef](#)]
72. Knipper, K.; Hogue, T.; Scott, R.; Franz, K. Evapotranspiration Estimates Derived Using Multi-Platform Remote Sensing in a Semiarid Region. *Remote Sens.* **2017**, *9*, 184. [[CrossRef](#)]
73. Scott, R.L. Using watershed water balance to evaluate the accuracy of eddy covariance evaporation measurements for three semiarid ecosystems. *Agric. For. Meteorol.* **2010**, *150*, 219–225. [[CrossRef](#)]
74. Taylor, K.E. Summarizing multiple aspects of model performance in a single diagram. *J. Geophys. Res. Atmos.* **2001**, *106*, 7183–7192. [[CrossRef](#)]
75. Chai, T.; Draxler, R.R. Root mean square error (RMSE) or mean absolute error (MAE)?—Arguments against avoiding RMSE in the literature. *Geosci. Model Dev.* **2014**, *7*, 1247–1250. [[CrossRef](#)]
76. Tabari, H.; Aeini, A.; Talaei, P.H.; Some'e, B.S. Spatial distribution and temporal variation of reference evapotranspiration in arid and semi-arid regions of Iran. *Hydrol. Process.* **2012**, *26*, 500–512. [[CrossRef](#)]
77. Wang, Z.; Schaaf, C.B.; Strahler, A.H.; Chopping, M.J.; Román, M.O.; Shuai, Y.; Woodcock, C.E.; Hollinger, D.Y.; Fitzjarrald, D.R. Evaluation of MODIS albedo product (MCD43A) over grassland, agriculture and forest surface types during dormant and snow-covered periods. *Remote Sens. Environ.* **2014**, *140*, 60–77. [[CrossRef](#)]
78. Cescatti, A.; Marcolla, B.; Vannan, S.K.S.; Pan, J.Y.; Román, M.O.; Yang, X.; Ciais, P.; Cook, R.B.; Law, B.E.; Matteucci, G. Intercomparison of MODIS albedo retrievals and in situ measurements across the global FLUXNET network. *Remote Sens. Environ.* **2012**, *121*, 323–334. [[CrossRef](#)]
79. Yang, W.; Tan, B.; Huang, D.; Rautiainen, M.; Shabanov, N.V.; Wang, Y.; Privette, J.L.; Huemmrich, K.F.; Fensholt, R.; Sandholt, I. MODIS leaf area index products: From validation to algorithm improvement. *IEEE Trans. Geosci. Remote Sens.* **2006**, *44*, 1885–1898. [[CrossRef](#)]
80. Chen, C.; Knyazikhin, Y.; Park, T.; Yan, K.; Lyapustin, A.; Wang, Y.; Yang, B.; Myneni, R.B. Prototyping of LAI and FPAR Retrievals from MODIS Multi-Angle Implementation of Atmospheric Correction (MAIAC) Data. *Remote Sens.* **2017**, *9*, 370. [[CrossRef](#)]
81. Yan, K.; Park, T.; Yan, G.; Liu, Z.; Yang, B.; Chen, C.; Nemani, R.R.; Knyazikhin, Y.; Myneni, R.B. Evaluation of MODIS LAI/FPAR Product Collection 6. Part 2: Validation and Intercomparison. *Remote Sens.* **2016**, *8*, 460. [[CrossRef](#)]

82. Ganguly, S.; Samanta, A.; Schull, M.A.; Shabanov, N.V.; Milesi, C.; Nemani, R.R.; Knyazikhin, Y.; Myneni, R.B. Generating vegetation leaf area index Earth system data record from multiple sensors. Part 2: Implementation, analysis and validation. *Remote Sens. Environ.* **2008**, *112*, 4318–4332. [[CrossRef](#)]
83. Yoon, Y.; Beighley, E.; Lee, H.; Pavelsky, T.; Allen, G. Estimating flood discharges in reservoir-regulated river basins by integrating synthetic SWOT satellite observations and hydrologic modeling. *J. Hydrol. Eng.* **2015**, *21*, 05015030. [[CrossRef](#)]
84. Nagler, P.L.; Cleverly, J.; Glenn, E.; Lampkin, D.; Huete, A.; Wan, Z. Predicting riparian evapotranspiration from MODIS vegetation indices and meteorological data. *Remote Sens. Environ.* **2005**, *94*, 17–30. [[CrossRef](#)]
85. Hashimoto, H.; Dungan, J.L.; White, M.A.; Yang, F.; Michaelis, A.R.; Running, S.W.; Nemani, R.R. Satellite-based estimation of surface vapor pressure deficits using MODIS land surface temperature data. *Remote Sens. Environ.* **2008**, *112*, 142–155. [[CrossRef](#)]
86. Tsuruta, K.; Kosugi, Y.; Takanashi, S.; Tani, M. Inter-annual variations and factors controlling evapotranspiration in a temperate Japanese cypress forest. *Hydrol. Process.* **2016**, *30*, 5012–5026. [[CrossRef](#)]



© 2017 by the authors. Licensee MDPI, Basel, Switzerland. This article is an open access article distributed under the terms and conditions of the Creative Commons Attribution (CC BY) license (<http://creativecommons.org/licenses/by/4.0/>).